PAPER

Check for updates

A semiconductive copper iodobismuthate hybrid: structure, optical properties and photocurrent response†

Jun Li, *[a,b] Ming-Hui Liu,[a] Hong-Yao Shen,[a] Meng-Zhen Liu,[a] Jin-Ting Wu[a] and Bo Zhang [ID] *[a,b]

Pursuits of new types of Pb-free heterometallic halides adequate for photovoltaic applications are still urgent but challenging. In this study, by using *in situ*-produced $[(Me)_2$-$(DABCO)]^{2+}$ (DABCO = 1,4-diazabicyclo[2.2.2]octane; Me = methyl) cations as structure-directing agents, we successfully constructed a non-perovskite copper iodobismuthate hybrid, namely $[(Me)_2$-$(DABCO)]_2Cu_2Bi_2I_{12}$ (**1**), which features discrete $[Cu_2Bi_2I_{12}]^{4-}$ anionic moieties formed by the building units of $[CuI_4]$ tetrahedra and $[BiI_6]$ octahedra. UV-Vis diffuse reflectance analyses showed that compound **1** possesses semiconductive behaviors with a narrow optical bandgap of 1.80 eV. More importantly, it exhibits excellent photoelectric switching abilities, and its photocurrent density (2.30 μA cm^{-2}) far exceeds those of some high-performance halide-based counterparts. Different from many heterometallic analogues, noteworthily, it also has dispersive band structure and strong electronic coupling near the Fermi level, resulting in a material with small effective masses that may be responsible for the good photoelectricity. This study may offer new guidance for the design and synthesis of eco-friendly heterometallic halides with unique structures and desirable properties.

Introduction

During the past few decades, iodoplumbate-based hybrids have drawn substantial attention owing to their distinctive structures and versatile applications in numerous fields, covering but not limited to semiconductors, white-light emission, photo/thermochroism and sewage purification.[1–6] In particular, the discovery of $[CH_3NH_3]PbI_3$ for solar cell devices has gained research interest.[7] However, the intrinsic toxicity and vulnerability to moisture may greatly hamper their further commercial applications, which motivated many researchers to pursue new environment-friendly and water-stable photoactive alternatives.

Among the numerous candidates, low-toxic Bi^{3+} appeared to be quite attractive due to its isoelectronic configuration with Pb^{2+} and strong spin–orbit coupling that are the mainstay for its remarkable optical behaviors. Another merit is that the iodobismuthate family also exhibits a variety of polymorphisms, which afford abundant possibilities to achieve or tailor

[a]College of Chemistry and Chemical Engineering, Liaocheng University, Liaocheng 252059, China. E-mail: junli@lcu.edu.cn, bzhang@lcu.edu.cn
[b]State Key Laboratory of Structural Chemistry, Fujian Institute of Research on the Structure of Matter, Chinese Academy of Sciences, Fuzhou 350002, China

the desired functionalities. The documented $[Bi_xI_y]^{(y-3x)-}$ anionic moieties ranged from some zero-dimensional (0D) clusters, one-dimensional (1D) chains and few two-dimensional (2D) layers, as exemplified by 0D-$[Bi_2I_8]^{2-}$, 0D-$[Bi_2I_{10}]^{4-}$, 0D-$[Bi_3I_{12}]^{3-}$, 0D-$[Bi_4I_{16}]^{4-}$, 0D-$[Bi_5I_{18}]^{3-}$, 0D-$[Bi_8I_{30}]^{6-}$, 1D-$[BiI_4]^{-}$, 1D-$[BiI_5]^{2-}$, 1D-$[Bi_4I_{14}]^{2-}$, 1D-$[Bi_6I_{22}]^{4-}$, 2D-$[Bi_{2/3}I_4]^{2-}$ and 2D-$[Bi_2I_7]^{-}$.[8–17] In order to further acquire more complicated motifs, an effective strategy is to design and fabricate heterometal iodobismuthates by embedding the second types of metal ions, typically monovalent Cu^+ and Ag^+. This huge progress had been demonstrated by $[C_{12}H_{18}N_2S_2]_2AgBiI_8$, $[C_3H_9NI]_4AgBiI_8$, $[APP]_4AgBiI_8 \cdot H_2O$, $[AMP]_4Ag_2Bi_2I_{16} \cdot H_2O$, $[C_6H_{16}N_2]_2CuBiI_8 \cdot 0.5H_2O$, $[C_6H_{16}N_2]_2$ $AgBiI_8 \cdot H_2O$, $[C_8H_{18}N]_4CuBiI_8$, $[C_6H_{16}N_2]_2CuBiI_8$, $[C_7H_{16}N]_4$ $CuBiI_8$, $[C_6H_{16}N_2]_2CuBiI_8 \cdot H_2O$, $[C_6H_{14}N]_4CuBiI_8 \cdot H_2O$, $[C_5H_{13}N_2]_4AgBiI_8 \cdot H_2O$ and $[H_2MPP]_2AgBiI_8$.[18–27] Nevertheless, most of the existing compounds crystallized in the common perovskite phases characteristic of octahedra in the corner-sharing mode only, and Cu/Ag–Bi–I compounds with novel structures have rarely been isolated to date. Thus, the quest for new types of heterometal iodobismuthates and in-depth understanding of their structure–performance relationships remained fascinating but challenging.

In this context, we used the DABCO ligands possessing both rigidity and flexibility to fortunately prepare a new member of the Cu–Bi–I family, namely, $[(Me)_2$-$(DABCO)]_2Cu_2Bi_2I_{12}$ (**1**). Interestingly, the as-synthesized

hybrid exhibits isolated $[Cu_2Bi_2I_{12}]^{4-}$ anions composed of $[CuI_4]$ tetrahedra and $[BiI_6]$ octahedra *via* face/edge-sharing. In particular, it also has the strong light-harvesting abilities with a narrow band gap (1.80 eV), demonstrating prominent photoelectric converting performances (2.30 μA cm^{-2}) under the alternating radiation of light. Theoretical studies further revealed that the dispersive band structure coordinated by strong electronic coupling renders compound **1** with smaller effective masses, which may be the main reason for its excellent optical behavior. The aqueous/thermal stability study and X-ray photoelectron spectroscopy (XPS), together with Hirshfeld surface analyses of the title compound, have also been performed.

Experimental section

Reagents and measurements

1,4-Diazabicyclo[2.2.2]octane (DABCO, Aladdin, 98%), BiI$_3$ (Adamas, 98%), CuI (Adamas, 99%), KI (Sinopharm, 99%), methanol (CH$_3$OH, Greagent, ≥99.5%) and HI (Adamas, 55–57%) were used in the experiment. All chemicals were directly used as received.

The thermal behavior of the title compound was studied using a NETZSCH STA449C unit (N$_2$ atmosphere, 10 K min^{-1}). Powder X-ray diffraction (PXRD) pattern was recorded using a SmartLab diffractometer. The compositional analyses including energy-dispersive X-ray (EDX) spectrum and X-ray photoelectron spectrum (XPS) were performed using a GX4 scanning electron microscope (Thermo Fisher) and an ESCALAB 250Xi analyzer (Thermo Fisher), respectively. SHIMADZU 3600 equipment was used to acquire UV-Vis diffuse reflectance spectra.

Synthesis of [(Me)$_2$-(DABCO)]$_2$Cu$_2$Bi$_2$I$_{12}$ (1)

DABCO (1.0 mmol, 0.112 g), BiI$_3$ (0.5 mmol, 0.295 g), CuI (1.0 mmol, 0.190 g), and KI (3.0 mmol, 0.498 g) were combined together in the presence of HI (4 mL) and CH$_3$OH (3 mL). The resulting mixture was transferred into a 20 mL Teflon-lined stainless steel reactor, which was kept at 140 °C for 5 days and then cooled to ambient temperature naturally. Dark-red sheet crystals of **1** were recovered in 21% yield based on BiI$_3$ by ethanol washing and air drying.

Photocurrent test

Photocurrent–time curves of the title compound were scanned on a CHI660E electrochemistry workstation equipped with a three-electrode configuration. During the measurement, a Pt wire, a Ag/AgCl electrode and a sample-coated ITO were adopted as the auxiliary, reference and working electrodes, respectively. For the preparation of the working electrode, 5 mg of microcrystalline powder was dispersed in a mixed ethanol/Nafion solution, followed by an ultrasonic treatment. Then, this slurry was dropped onto a pre-polished ITO substrate and dried naturally at ambient temperature. The electrolyte was 0.1 M KCl aqueous solution. A 300 W Xe lamp with/

without a 420 nm filter was utilized as the simulated visible-light and full-spectrum illumination source.

X-ray crystallography

Crystallographic data of compound **1** were recorded using a Bruker SMART CCD-based diffractometer with Mo Kα radiation (λ = 0.71073 Å) at 298(2) K. The direct method structure solution and full-matrix least-squares refinement against F^2 were performed using the SHELXS-2014 program.[28] All atoms but hydrogen were anisotropically refined, while the hydrogen atoms of organic molecules were theoretically generated with fixed thermal factors. The structural refinement details of the title compound are provided in Table 1, and important bond lengths/angles are listed in Tables S1 and S2.†

Computational methodology

The theoretical studies of compound **1** involving band structure and density of states (DOS) were performed by density functional theory (DFT) calculations, implemented in the VASP code. During the calculation, the exchange–correlation interactions were described *via* the Perdew–Burke–Ernzerhof (PBE) generalized gradient approximation (GGA).[29] Cu 3d^{10}4s^1, Bi 6s^{2}6p^3, I 5s^{2}5p^5, C 2s^{2}2p^3, N 2s^{2}2p^4, and H 1s^1 were treated as the valence electrons of the title compound. The kinetic energy cutoff of plane-wave was fixed to 500 eV and the Monkhorst–Pack k-point mesh was set as 2 × 6 × 4.

Results and discussion

Structural description

Compound **1**, formulated as $[(Me)_2-(DABCO)]_2Cu_2Bi_2I_{12}$, crystallizes in the monoclinic $C2/c$ (no. 15) space group and takes

Table 1 Crystallographic data of compound 1

Compound	**1**
Formula	C$_{16}$H$_{36}$Bi$_2$Cu$_2$I$_{12}$N$_4$
f_w	2352.33
Crystal system	Monoclinic
Space group	$C2/c$
a/Å	28.132(3)
b/Å	9.2296(9)
c/Å	16.8237(15)
β/°	94.638(2)
V/Å^3	4353.9(7)
Z	4
λ/Å	0.71073
ρ_{calcd}/g cm^{-3}	3.589
μ/mm^{-1}	17.548
$F(000)$	4080
Measured refls.	9841
Independent refls.	3801
No. of parameters	166
R_{int}	0.0664
GOF	1.078
R_1 $[I > 2\sigma(I)]^a$	0.0611
w$R(F_2)$ $[I > 2\sigma(I)]^b$	0.1689
CCDC	2183662

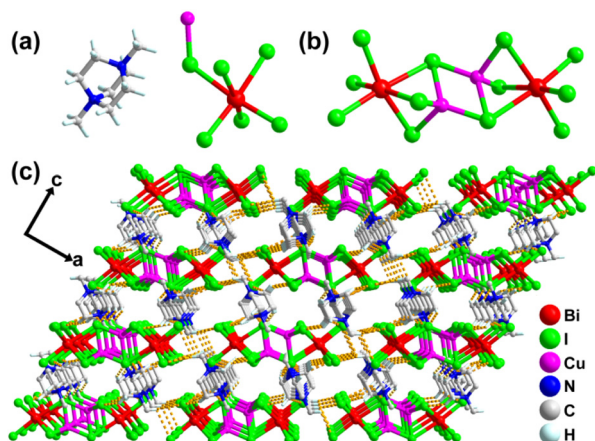$^a R_1 = \sum||F_o| - |F_c||/\sum|F_o|$. $^b wR_2 = [\sum w(F_o^2 - F_c^2)^2/\sum w(F_o^2)^2]^{1/2}$.

Fig. 1 (a) Asymmetric unit of compound **1**. (b) [Cu$_2$Bi$_2$I$_{12}$]$^{4-}$ anion. (c) Perspective view of compound **1** along the *b* axis, in which the dashed lines show C–H⋯I interactions.

a discrete anionic moiety of [Cu$_2$Bi$_2$I$_{12}$]$^{4-}$ (Fig. 1). Its asymmetric unit comprises half of the formula unit, *i.e.*, one crystallographically distinguished Cu$^+$ ion, one Bi^{3+} ion, six I$^-$ ions and one [(Me)$_2$-(DABCO)]$^{2+}$ cation (Fig. 1a). In the [Cu$_2$Bi$_2$I$_{12}$]$^{4-}$ anions, the Cu$^+$ ions are four-coordinated, giving the distorted tetrahedral configurations. This is quite different from the [CuI$_6$] octahedra found in [C$_7$H$_{16}$N]$_4$CuBiI$_8$, [C$_6$H$_{16}$N$_2$]$_2$CuBiI$_8$·H$_2$O, [C$_6$H$_{16}$N$_2$]$_2$CuBiI$_8$·0.5H$_2$O, and [C$_6$H$_{14}$N]$_4$CuBiI$_8$·H$_2$O.[21,22] The Cu–I bond lengths and I–Cu–I bond angles vary from 2.560(3) to 2.700(4) Å and 99.30(12) to 120.85(15)°, respectively. The Bi^{3+} ions adopt a typical octahedral [BiI$_6$] geometry, with the Bi–I bond distances in the range of 2.9288(16)–3.3066(16) Å. Noteworthily, there are three kinds of I$^-$ ions in the structure, involving the terminal styles (I(2), I(3) and I(6)), μ$_2$-bridging linkers (I(4) and I(5)) and μ$_3$-connecting modes (I(1)). These

coordination behaviors and observed data of bond distances/ angles are normal and call for no more comments.

As depicted in Fig. 1b, one [CuI$_4$] tetrahedron and one [BiI$_6$] octahedron are interconnected *via* edge-sharing to create a [CuBiI$_7$] dimer. Then, two centrosymmetric [CuBiI$_7$] units are further condensed by I(1) atoms to form the [Cu$_2$Bi$_2$I$_{12}$]$^{4-}$ anion, which resembles the [A$_2$Bi$_2$I$_{12}$]$^{4-}$ (A = Cu and Ag) ones in [PPh$_4$]$_4$Cu$_2$Bi$_2$I$_{12}$, [PPh$_4$]$_4$Ag$_2$Bi$_2$I$_{12}$, [Ni(bipy)$_3$]$_2$Ag$_2$Bi$_2$I$_{12}$, and [Fe(bipy)$_3$]$_2$Ag$_2$Bi$_2$I$_{12}$.[26,30] At the same time, the neighboring Cu⋯Cu separations reached 2.597(8) Å, lesser than twice the vdW radius of Cu (2.80 Å), implying the existence of relatively obvious cuprophilic interactions.[31–33] The *in situ*-generated [(Me)$_2$-(DABCO)]$^{2+}$ cations acting as charge-balancing agents separated the above-mentioned [Cu$_2$Bi$_2$I$_{12}$]$^{4-}$ anions, resulting in a 3D supermolecular network *via* extensive hydrogen bond interactions (Fig. 1c). The C–H⋯I contacts scatter from 3.71(2) to 3.984(18) Å and 111.5 to 159.5°, respectively.

Hirshfeld surface analyses

To clearly present and quantitatively describe the intermolecular forces existing in the structure, we conducted the Hirshfeld surface analyses for the title compound. Overall, the sky-blue points in the full fingerprint plot scattered widely, with the majority of tips at 2.4 ≤ d_e + d_i ≤ 5.8 Å (Fig. 2a). Decomposition plots further revealed that the most significant interaction in compound **1** was H⋯I/I⋯H contact, accounting for 78.6% of the total Hirshfeld surface. As illustrated in Fig. 2b, it emerged like two wings of a bird, with the proportion in the bottom right and top left reaching 49.1% and 29.5%, respectively. The high occupancy rate indicated that the interactions associated with hydrogen bonds exerted an important role in stabilizing its structural construction. For compound **1**, the second contributor is responsible for the non-covalent Cu⋯I/I⋯Cu contact, which appeared like a
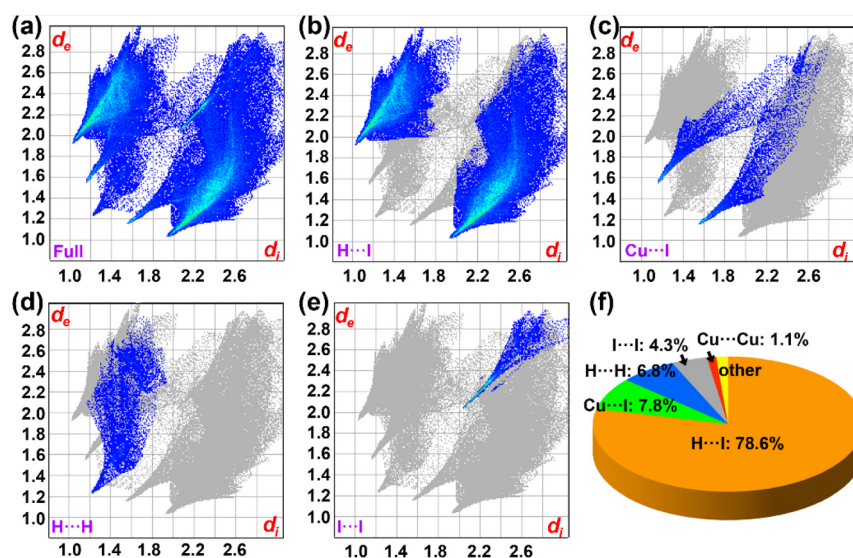

Fig. 2 Two-dimensional fingerprint plot of compound **1**: (a) full interactions; (b) H⋯I interactions; (c) Cu⋯I interactions; (d) H⋯H interactions; (e) I⋯I interactions; and (f) contribution percentages of various interactions.

pincer with a ratio of 7.8% (Fig. 2c). Different from many documented metal halides (*e.g.*, $[Fe(bipy)_3]AgBiI_6$, $[Co(bipy)_3]_2Ag_4Bi_2I_{16}$, $[Zn(bipy)_3]_2Ag_2BiI_6(I)_{1.355}(I_3)_{1.645}$, $[NH_4][Fe(bipy)_3]_2Ag_6Br_{11}$ and $[Pb(MCP)_2I]PbI_3$,[30,34–37] the dominance of H⋯H interaction occurred on only one side of the fingerprint plot, with a proportion of 6.8% (Fig. 2d). In addition, the I⋯I contact in compound **1** was also negligible, contributing 4.3% to the Hirshfeld surface (Fig. 2e). The comparisons with some other interactions are depicted in Fig. 2f.

Structural characterizations

The PXRD measurement showed that the experimental pattern of compound **1** coincided with the simulated one, suggesting the high purity of the as-prepared sample (Fig. 3a). Moreover, it can keep its robust framework despite the continuous immersion in water for 24 h, which provided the prerequisite adequate for the practical photovoltaic applications. The thermal stability of compound **1** was also impressive, with the weight loss occurring at approximately 200 °C (Fig. 3b). This is obviously superior to many low-dimensional halide counterparts such as $[Cu(CH_3CN)_4]_2Cu_2Bi_2I_{10}$, $[MePy]_3Bi_2I_9·(I_2)_3$, $[La(DMSO)_8]Bi_2I_9$, $[DHEP]SbCl_5·2H_2O$, $[TMPDA]ZnBr_4$ and $[DPA]_3InCl_6$,[25,38–42] the decomposition temperature of which was customarily as low as 150 °C. Then, we further investigated its chemical composition by EDX and XPS analyses (Fig. S4–S6† and Fig. 3c). In these two tests, the expected Cu, Bi and I elements are both observed in compound **1**. The high-resolution Bi-4f spectrum, depicted in Fig. 3d, contained two single peaks centered at 164.1 and 158.8 eV, which are characteristic of $4f_{5/2}$ and $4f_{7/2}$ states of Bi^{3+}, respectively. These observed binding energies are well in line with some documented analogues, including but not limited to $[CH_3NH_3]_3Bi_2I_9$, $(R-MBA)_2Bi_2I_8$, $[NH_4][Ni(phen)_3]BiI_6$, $[Zn(bipy)_3]_2Ag_2BiI_6(I)_{1.355}(I_3)_{1.645}$ and $[Co(bipy)_3]_2Ag_4Bi_2I_{16}$.[34,35,43–45]

The other results for Cu and I compositions are also normal calling no more statements.

Optical properties

The UV-Vis diffuse reflection spectrum of the title compound was recorded using a powder sample at room temperature. As presented in Fig. 4a, compound **1** displays a sharp optical absorption edge at about 688 nm, indicating the visible light responding semiconductor property. According to the Tauc function, its band gap was determined to be 1.80 eV (Fig. 4b), which is in accordance with the color of dark-red and narrower than those of many high-performance light absorbers (Fig. 4c). Representative examples include $[La(DMSO)_8]Bi_2I_9$ (2.21 eV), $[Bi(DMSO)_8]Bi_2I_9$ (2.17 eV), $[AmV]BiI_5$ (1.54 eV), $[PiC_2]_2Bi_2I_{10}$ (2.08 eV), PiC_5BiI_5 (1.73 eV), $[PiC_5]_2Bi_4I_{16}$ (2.10 eV), $[HpipeH_2]_2Bi_2I_{10}·2H_2O$ (1.80 eV), $LiBiI_4·5H_2O$ (1.70 eV), $KBiI_4·H_2O$ (1.76 eV), $[CH_3NH_3]_3Bi_2Br_9$ (2.50 eV), $[H_2MPP]_2AgBiI_8$ (2.26 eV), $[APP]_4AgBiI_8·H_2O$ (2.12 eV), $[AMP]_4AgBiI_8·H_2O$ (2.07 eV), $[Ni(bipy)_3]AgBiBr_6$ (2.06 eV), $[NH_4]_3Bi_2I_9$ (2.04 eV), $[C_8H_{20}N]_2Ag_2Bi_4I_{16}$ (1.93 eV) and $[Et_4N]_2Cu_2Bi_2I_{10}$ (1.89 eV).[16,20,23–25,30,39,46–50]

Mott–Schottky plots were used to further study the optical behavior of the title compound. As shown in Fig. 4d, the positive slope of the obtained $C^{2−}$ to the potential plot was consistent with those of typical n-type semiconductors. The flat band position (V_{fb}) determined from the intersection is approximately −0.34 V *vs.* Ag/AgCl. Since it is generally accepted that the bottom of the conduction band in many n-type semiconductors is approximately equal to the flat band potential, and the conduction band (CB) of the title compound was estimated to be −0.14 V *vs.* NHE. With the band gap energy (E_g) of the title compound estimated to be 1.80 eV, its valence band (VB) was then calculated to be 1.56 V *vs.* NHE.
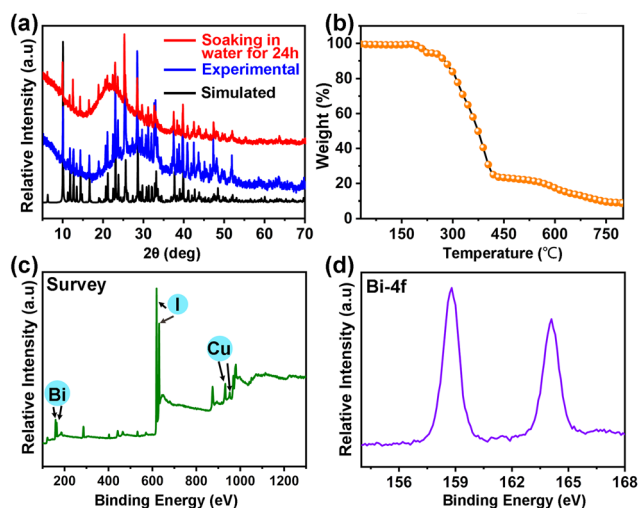
Fig. 3 (a) PXRD patterns of compound **1**. (b) TGA curve of compound **1**. (c) XPS survey spectrum of compound **1**. (d) High-resolution Bi-4f peaks of compound **1**.

Fig. 4 (a) UV-Vis adsorption spectrum of compound **1**. (b) UV-Vis diffuse reflection spectrum of compound **1**. (c) Band-gap energy of compound **1** as compared to some Bi-based metal halides. (d) Mott–Schottky plots for compound **1**. Inset: energy diagram of the HOMO and LUMO levels.

Photoelectric switching performances

Given the narrow energy gap (1.80 eV) of compound **1**, we further explored its applicability as a potential photoelectric active material. The time-dependent photocurrent curves with on–off models are recorded in Fig. 5. Under the periodic on/off visible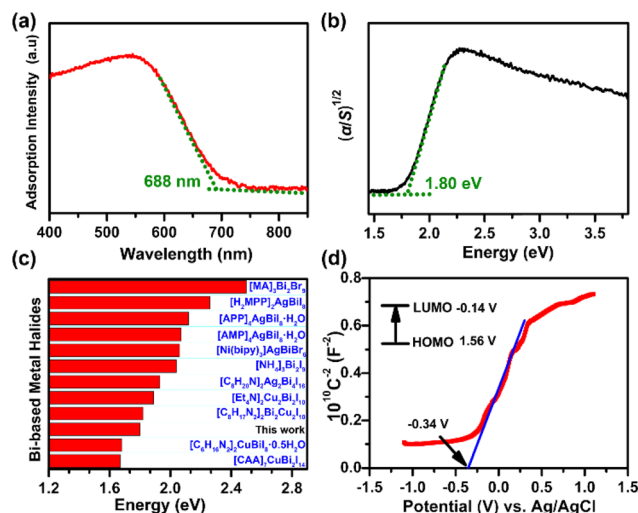 light irradiation, compound **1** was found to have prompt and reproducible photocurrent response, with the steady transient photocurrent intensity achieved around 2.30 μA cm^{-2} (Fig. 5a). In particular, such a value is well comparable or largely outperforms those of many high-performance halide counterparts (*e.g.*, [C$_6$H$_{14}$N]$_4$CuBiI$_8$·H$_2$O, [C$_6$H$_{16}$N$_2$]$_2$AgBiI$_8$·H$_2$O, [Mn(bipy)$_3$]$_2$Pb$_8$I$_{21}$, [Ni(phen)$_3$]Pb$_2$I$_6$·CH$_3$CN, [Fe(phen)$_3$]$_2$Ag$_3$Pb$_2$I$_{11}$, [Pr(bpdo)$_3$(H$_2$O)]Bi$_2$I$_9$ and [Fe(phen)$_3$]Ag$_2$PbBr$_6$),[21,22,51–55] manifesting the good transport efficiency of carriers. In addition, it exhibits no conspicuous decays in contempt of the repeatable illumination, demonstrating the potential for practical photovoltaic applications. Its photocurrent density signal can be further improved (8.20 μA cm^{-2}) as the designed electrode was subjected to the full-spectrum environment (Fig. 5b). This is reasonable and may be ascribed to the more photo-generated hole/electron pairs due to the enhanced light harvesting ability, which has also appeared in the instance of [NH$_4$][Fe(bipy)$_3$]$_2$Ag$_6$Br$_{11}$, [Fe(bipy)$_3$]AgBiI$_6$, [Pb(MCP)$_2$I]PbI$_3$, [Co(bipy)$_3$]$_2$[AgBiBr$_7$][Bi$_2$Br$_9$]·H$_2$O, [Zn(phen)$_3$]$_2$[Ag$_2$Bi$_2$I$_{12}$], [Zn(bipy)$_3$]$_2$Ag$_2$BiI$_6$(I)$_{1.355}$(I$_3$)$_{1.645}$ and [Co(bipy)$_3$]$_2$Ag$_4$Bi$_2$I$_{16}$.[30,34–37,56] These behaviors displayed by compound **1** make it a new and promising semiconducting photodetector.
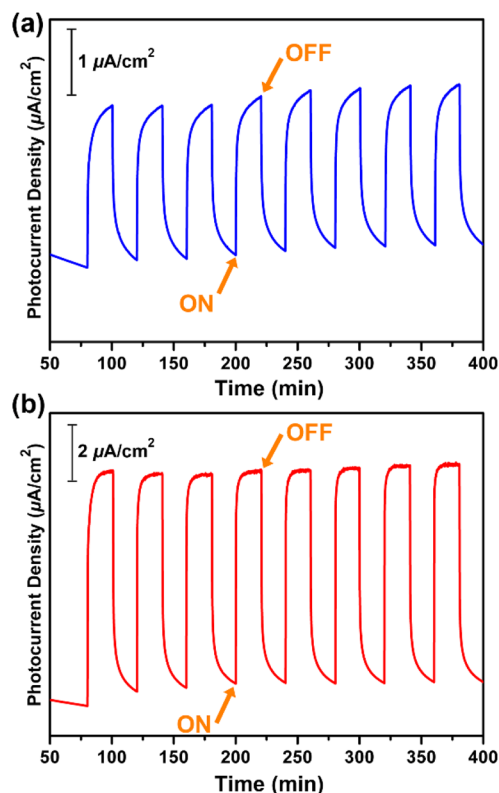

Fig. 5 Time-dependent photocurrent curves under the alternate radiation: (a) visible light. (b) Full-spectrum light.

Theoretical study

To better elucidate the origin of optical and optoelectronic properties, the electronic structure calculations of the title compound on the basis of DFT were done (Fig. 6). Band alignments revealed that compound **1** exhibits the indirect-band-gap semiconductor character, with the lowest energy of conduction bands (CBs) and the highest energy of valence bands (VBs) localized at the Γ point and E point, respectively (Fig. 6a). Its theoretical band value was estimated to be 1.25 eV, which is smaller than the experimental result of 1.80 eV. Such a discrepancy is normal and can be attributed to the well-known self-interaction error of the PBE density functional.[29] Notably, compound **1** also possesses the dispersive band distributions, in particular the CBs, indicating the strong intermolecular electronic coupling between the neighboring species. This is distinctly different from some documented metal halide counterparts (*e.g.*, [NH$_4$][Fe(bipy)$_3$]$_2$Ag$_6$Br$_{11}$, [Fe(phen)$_3$]Ag$_2$PbBr$_6$, [NH$_4$][Ni(phen)$_3$]BiI$_6$, [Zn(bipy)$_3$]$_2$Ag$_2$BiI$_6$(I)$_{1.355}$(I$_3$)$_{1.645}$, [Co(bipy)$_3$]$_2$Ag$_4$Bi$_2$I$_{16}$ and [Zn(phen)$_3$]$_2$Ag$_2$Bi$_2$I$_{12}$),[34–36,45,55,56] which are characteristic of large organic moieties and routinely feature the relative flat band compositions. In terms of the DOS diagram, we can see that its VB maximum was dominated by the Cu-3d and I-5p states, while the CB minimum was nearly from the Bi-6p and I-5p orbitals (Fig. 6b and Fig. S7†). The regions far from the Fermi level, in particular −5.0 to −10.0 eV, mostly stemmed from the [(Me)$_2$-(DABCO)]$^{2+}$ cations (Fig. 6b and Fig. S7†). These results clearly indicate that the organic cations in compound **1** made almost no contributions to the Frontier orbitals, which resemble the case of the classical perovskite material [CH$_3$NH$_3$]PbI$_3$.[57] This can also be visualized by the wave function maps, that is, the VB maximum and CB minimum projected onto Cu–I antibonding and Bi–I antibonding orbitals (Fig. 6c and d). Therein, the stronger antibonding coupling between the Bi-p orbital and the I-p orbital contributes to the more dispersive conduction band. It is known that the relative dispersive band structure favors the generation of smaller carrier effective mass. Consequently, the intrinsic optical absorption of the title compound can be responsible for the charge transitions occurring within the inorganic [Cu$_2$Bi$_2$I$_{12}$]$^{4-}$ anions.

In addition, we further evaluated the carrier effective masses of the title compound. As provided in Table 2, the calculated effective masses for electrons along Γ–Z and Γ–Y directions are 0.28m_0 and 0.30m_0 (m_0 is the free electron mass), respectively. The hole effective masses were found to be 3.33m_0 (E–D) and 0.15m_0 (E–C). These results were well comparable to the cases of [CH$_3$NH$_3$]PbI$_3$ (0.23m_0 and 0.29m_0 respectively) and [CH$_3$NH$_3$]$_2$Pb(SCN)$_2$I$_2$ (0.14m_0 and 0.20m_0 respectively),[57,58] and far less than those of [Fe(bipy)$_3$]AgBiI$_6$ (16.67m_0 and 1.29m_0 respectively),[30] indicating the good carrier transport potentials in compound **1**. The smaller effective masses, together with strong optical absorption, render it with relatively satisfying photoelectric performances.
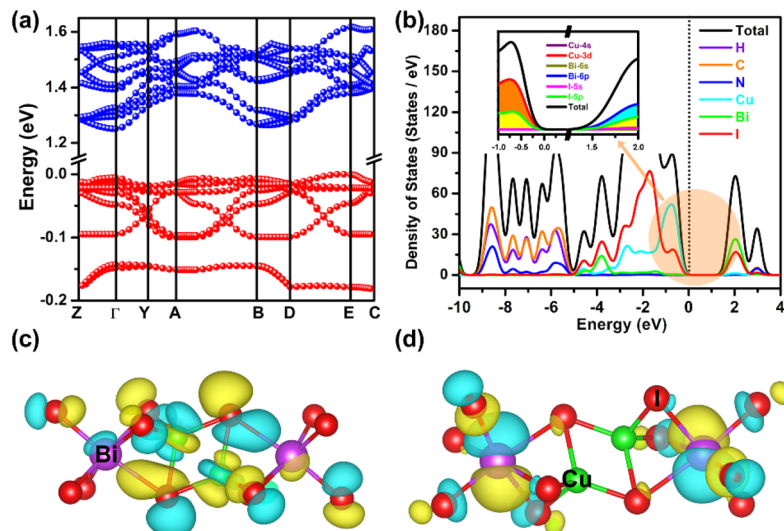
Fig. 6 Band structure (a) and DOS (b) diagram of compound **1**. The electron wave function maps of VB maximum (c) and CB minimum (d) of compound **1**.

Table 2 Effective masses of electrons and holes for compound **1**

CBs	Direction	$m_{\text{e}}^{*}/m_{\text{o}}$	VBs	Direction	$m_{\text{h}}^{*}/m_{\text{o}}$
Γ	Γ–Z	0.28	E	E–D	3.33
	Γ–Y	0.30		E–C	0.15

Conclusion

In summary, a new $[(\text{Me})_2\text{-(DABCO)}]^{2+}$-templated copper iodo-bismuthate hybrid characteristic of discrete $[\text{Cu}_2\text{Bi}_2\text{I}_{12}]^{4-}$ anionic moieties, namely, $[(\text{Me})_2\text{-(DABCO)}]_2\text{Cu}_2\text{Bi}_2\text{I}_{12}$, has been solvothermally fabricated and structurally characterized. Attractively, the prepared hybrid possesses good moisture stability, strong visible light absorption and excellent photoelectric switching performance, which may be attributable to the significant electronic coupling in both the conduction band and the valence band. This work may provide an insight into obtaining new types of organic–inorganic hybrid metal halides with promising photovoltaic properties. More related exploration of the syntheses and in-depth understanding of their structure–activity relationships is in progress in our group.

Conflicts of interest

There are no conflicts to declare.

Acknowledgements

References

1 T. M. Brenner, D. A. Egger, L. Kronik, G. Hodes and D. Cahen, *Nat. Rev. Mater.*, 2016, **1**, 15007.

2 L. L. Mao, P. J. Guo, M. Kepenekian, I. Hadar, C. Katan, J. Even, R. D. Schaller, C. C. Stoumpos and M. G. Kanatzidis, *J. Am. Chem. Soc.*, 2018, **140**, 13078–13088.

3 Z. J. Zhang, S. C. Xiang, G. C. Guo, G. Xu, M. S. Wang, J. P. Zou, S. P. Guo and J. S. Huang, *Angew. Chem., Int. Ed.*, 2008, **47**, 4149–4152.

4 X. L. Song, G. F. Wei, J. Sun, C. D. Peng, J. L. Yin, X. Zhang, Y. L. Jiang and H. H. Fei, *Nat. Catal.*, 2020, **3**, 1027–1033.

5 P. F. Chen, W. J. Ong, Z. H. Shi, X. J. Zhao and N. Li, *Adv. Funct. Mater.*, 2020, **30**, 1909667.

6 J. Q. Zhao, H. S. Shi, L. R. Zeng, H. Ge, Y. H. Hou, X. M. Wu, C. Y. Yue and X. W. Lei, *Chem. Eng. J.*, 2022, **431**, 134336.

7 A. Kojima, K. Teshima, Y. Shirai and T. Miyasaka, *J. Am. Chem. Soc.*, 2009, **131**, 6050–6051.

8 L. M. Wu, X. T. Wu and L. Chen, *Coord. Chem. Rev.*, 2009, **253**, 2787–2804.

9 S. A. Adonin, M. N. Sokolov and V. P. Fedin, *Coord. Chem. Rev.*, 2016, **312**, 1–21.

10 N. Dehnhardt, J. N. Luy, M. Szabo, M. Wende, R. Tonner and J. Heine, *Chem. Commun.*, 2019, **55**, 14725–14728.

11 D. B. Mitzi, *Inorg. Chem.*, 2000, **39**, 6107–6113.

12 A. M. Goforth, M. A. Tershansy, M. D. Smith, L. Peterson, J. G. Kelley, W. J. I. DeBenedetti and H. C. zur Loye, *J. Am. Chem. Soc.*, 2011, **133**, 603–612.

13 M. Q. Li, Y. Q. Hu, L. Y. Bi, H. L. Zhang, Y. Y. Wang and Y. Z. Zheng, *Chem. Mater.*, 2017, **29**, 5463–5467.

14 W. C. Zhang, X. T. Liu, L. N. Li, Z. H. Sun, S. G. Han, Z. Y. Wu and J. H. Luo, *Chem. Mater.*, 2018, **30**, 4081–4088.

15 D. Chen, S. Hao, L. Fan, Y. Guo, J. Yao, C. Wolverton, M. G. Kanatzidis, J. Zhao and Q. Liu, *Chem. Mater.*, 2021, **33**, 8106–8111.

16 A. Skorokhod, N. Mercier, M. Allain, M. Manceau, C. Katan and M. Kepenekian, *Inorg. Chem.*, 2021, **60**, 17123–17131.

17 X. Zhang, P. Zhang, Y. G. Weng, Z. Z. Tang, Q. Y. Zhu and J. Dai, *Inorg. Chem.*, 2018, **57**, 11113–11122.

18 M. K. Jana, S. M. Janke, D. J. Dirkes, S. Dovletgeldi, C. Liu, X. X. Qin, K. Gundogdu, W. You, V. Blum and D. B. Mitzi, *J. Am. Chem. Soc.*, 2019, **141**, 7955–7964.

19 Y. P. Yao, B. Kou, Y. Peng, Z. Y. Wu, L. N. Li, S. S. Wang, X. Y. Zhang, X. T. Liu and J. H. Luo, *Chem. Commun.*, 2020, **56**, 3206–3209.

20 M. S. Lassoued, L. Y. Bi, Z. X. Wu, G. J. Zhou and Y. Z. Zheng, *J. Mater. Chem. C*, 2020, **8**, 5349–5354.

21 L. Y. Bi, T. L. Hu, M. Q. Li, B. K. Ling, M. S. Lassoued, Y. Q. Hu, Z. X. Wu, G. J. Zhou and Y. Z. Zheng, *J. Mater. Chem. A*, 2020, **8**, 7288–7296.

22 L. Y. Bi, Y. Q. Hu, M. Q. Li, T. L. Hu, H. L. Zhang, X. T. Yin, W. X. Que, M. S. Lassoued and Y. Z. Zheng, *J. Mater. Chem. A*, 2019, **7**, 19662–19667.

23 M. S. Lassoued, T. B. Wang, A. Faizan, Q. W. Li, W. P. Chen and Y. Z. Zheng, *J. Mater. Chem. C*, 2022, **10**, 12574–12581.

24 W. X. Chai, L. M. Wu, J. Q. Li and L. Chen, *Inorg. Chem.*, 2007, **46**, 1042–1044.

25 W. X. Chai, L. M. Wu, J. Q. Li and L. Chen, *Inorg. Chem.*, 2007, **46**, 8698–8704.

26 N. Dehnhardt, H. Borkowski, J. Schepp, R. Tonner and J. Heine, *Inorg. Chem.*, 2018, **57**, 633–640.

27 Y. H. Cai, A. M. Chippindale, R. J. Curry and P. Vaqueiro, *Inorg. Chem.*, 2021, **60**, 5333–5342.

28 G. M. Sheldrick, *Acta Crystallogr., Sect. A: Found. Adv.*, 2015, **71**, 3–8.

29 G. Kresse and J. Furthmuller, *Phys. Rev. B: Condens. Matter Mater. Phys.*, 1996, **54**, 11169–11186.

30 B. Zhang, J. Li, M. Pang, Y. S. Wang, M. Z. Liu and H. M. Zhao, *Inorg. Chem.*, 2022, **61**, 406–413.

31 A. Bondi, *J. Phys. Chem.*, 1964, **68**, 441–451.

32 S. Sculforta and P. Braunstein, *Chem. Soc. Rev.*, 2011, **40**, 2741–2760.

33 P. K. Mehrotra and R. Hoffmann, *Inorg. Chem.*, 1978, **17**, 2187–2189.

34 B. Zhang, J. Li, M. Pang, X. Chen and M. Z. Liu, *Inorg. Chem.*, 2022, **61**, 9808–9815.

35 B. Zhang, J. Li, Y. Yang, W. H. Wang, H. Y. Shen and Y. N. Shao, *Dalton Trans.*, 2022, **51**, 13361–13367.

36 B. Zhang, J. Li, X. Chen, M. F. Yang, H. Y. Shen and J. C. Zhu, *Inorg. Chem. Commun.*, 2022, **137**, 109250.

37 B. Zhang, J. Li, L. Z. Li, X. C. Ren, M. Pang and Y. N. Shao, *Cryst. Growth Des.*, 2021, **21**, 5317–5324.

38 A. N. Usoltsev, N. A. Korobeynikov, A. S. Novikov, P. E. Plyusnin, B. A. Kolesov, V. P. Fedin, M. N. Sokolov and S. A. Adonin, *Inorg. Chem.*, 2020, **59**, 17320–17325.

39 P. F. Hao, W. P. Wang, J. J. Shen and Y. L. Fu, *Dalton Trans.*, 2020, **49**, 1847–1853.

40 D. Y. Li, J. H. Song, Z. Y. Xu, Y. J. Gao, X. Yin, Y. H. Hou, L. J. Feng, C. Y. Yue, H. H. Fei and X. W. Lei, *Chem. Mater.*, 2022, **34**, 6985–6995.

41 Y. Y. Ma, Y. M. Sun, W. J. Xu, X. L. Liu, Q. Q. Zhong, Y. R. Song, H. Q. Fu, C. Y. Yue and X. W. Lei, *Adv. Opt. Mater.*, 2022, 2200386.

42 C. Sun, J. P. Zang, Y. Q. Liu, Q. Q. Zhong, X. X. Xing, J. P. Li, C. Y. Yue and X. W. Lei, *CCS Chem.*, 2022, **4**, 3106–3121.

43 Y. M. Guo, G. N. Liu, Z. X. Li, Y. B. Lou, J. X. Chen and Y. X. Zhao, *ACS Sustainable Chem. Eng.*, 2019, **7**, 15080–15085.

44 Z. Li, Y. Yan, M. S. Song, J. Y. Xin, H. Y. Wang, H. Wang and Y. Wang, *J. Phys. Chem. Lett.*, 2022, **13**, 4073–4081.

45 X. C. Ren, J. Li, W. H. Wang, X. Chen, B. Zhang and L. Z. Li, *Inorg. Chem. Commun.*, 2021, **130**, 108714.

46 V. Y. Kotov, A. B. Ilyukhin, A. A. Korlyukov, A. F. Smol'yakov and S. A. Kozyukhin, *New J. Chem.*, 2018, **42**, 6354–6363.

47 T. A. Shestimerova, A. V. Mironov, M. A. Bykov, A. V. Grigorieva, Z. Wei, E. V. Dikarev and A. V. Shevelkov, *Molecules*, 2020, **25**, 2765.

48 N. A. Yelovik, A. V. Mironov, M. A. Bykov, A. N. Kuznetsov, A. V. Grigorieva, Z. Wei, E. V. Dikarev and A. V. Shevelkov, *Inorg. Chem.*, 2016, **55**, 4132–4140.

49 M. Leng, Z. Chen, Y. Yang, Z. Li, K. Zeng, K. Li, G. Niu, Y. He, Q. Zhou and J. Tang, *Angew. Chem., Int. Ed.*, 2016, **55**, 15012–15016.

50 R. Z. Zhuang, X. J. Wang, W. B. Ma, Y. H. Wu, X. Chen, L. H. Tang, H. M. Zhu, J. Y. Liu, L. L. Wu, W. Zhou, X. Liu and Y. Yang, *Nat. Photonics*, 2019, **13**, 602–608.

51 C. Y. Yue, Y. D. Yue, H. X. Sun, D. Y. Li, N. Lin, X. M. Wang, Y. X. Jin, Y. H. Dong, Z. H. Jing and X. W. Lei, *Chem. Commun.*, 2019, **55**, 6874–6877.

52 B. Zhang, H. Y. Sun, J. Li, Y. R. Xu, Y. P. Xu, X. Yang and G. D. Zou, *Dalton Trans.*, 2020, **49**, 1803–1810.

53 M. Pang, X. C. Ren, X. Chen, H. Y. Shen, J. Li, B. Zhang and L. Z. Li, *Inorg. Chem. Commun.*, 2022, **139**, 109342.

54 Y. He, Y. R. Huang, Y. L. Li, H. H. Li, Z. R. Chen and R. Jiang, *Inorg. Chem.*, 2019, **58**, 13862–13880.

55 X. C. Ren, J. Li, W. H. Wang, Y. N. Shao, B. Zhang and L. Z. Li, *J. Solid State Chem.*, 2022, **308**, 122912.

56 B. Zhang, Y. N. Wang, J. Li, X. C. Ren, Y. Yang and X. R. Yang, *Cryst. Growth Des.*, 2022, **22**, 7434–7442.

57 G. Giorgi, J. Fujisawa, H. Segawa and K. Yamashita, *J. Phys. Chem. Lett.*, 2013, **4**, 4213–4216.

58 A. M. Ganose, C. N. Savory and D. O. Scanlon, *J. Mater. Chem. A*, 2017, **5**, 7845–7853.